A sustainable approach to energy storage in buildings: the first rechargeable geopolymer-based battery

Vadim Kovrugin, Liliane Guerlou-Demourgues, Laurence Croguennec, Jorge Dolado, Cyril Aymonier

COMMUNICATION

A Sustainable Approach to Energy Storage in Buildings: the First Rechargeable Geopolymer-based Battery

Received 00th January 20xx,
Accepted 00th January 20xx

DOI: 10.1039/x0xx00000x

Vadim M. Kovrugin,*[a,b,c] Liliane Guerlou-Demourgues,[a,c] Laurence Croguennec,[a,c,d] Jorge S. Dolado,[e] and Cyril Aymonier[a,c,d]

This study presents a novel metakaolin-based geopolymer rechargeable battery with Zn as negative electrode and MnO_2 as positive electrode, demonstrating superior energy storage performance of about 3.3 Wh/L. Despite challenges, our findings highlight the potential for integrating energy storage into building materials, paving the way for sustainable infrastructure development.

1 Introduction

The investigation of building materials by electrochemical techniques is not new. Along with the main objective of these analyses, this approach makes it possible to discover new applications in the energy sector. For instance, a study conducted in 1966 examined the setting time of cement paste by assembling essentially one of the first reported galvanic batteries, composed of a copper positive electrode, a lead negative electrode, and fresh cement, which produced a voltage of nearly 300 mV.[1] In the XXIst century, the increasing demand for integrating renewable energy sources into the energy grid and the need for sustainable infrastructure make the development of efficient and eco-friendly energy storage systems essential. Since the first cement batteries in 1960s, and after a relatively long period marked by significant discoveries in electrochemical energy storage,[2,3] researchers have renewed their interest in storing energy in materials used in construction such as, *e.g.*, electroceramics,[4] thermal batteries[5] and thermal energy storage.[6,7] By seamlessly integrating such solutions within cementitious matrices, these devices may offer a unique opportunity to store and harness electrical energy directly within the built environment. This approach not only optimizes space utilization but also provides a sustainable and decentralized energy storage solution. However, the design and fabrication of cement-based energy devices must involve the careful selection of materials that exhibit both structural integrity and electrical activity.

Although cement-like materials have not traditionally been considered suitable for efficient electrochemical energy storage applications, they are also now being explored as potential sustainable complementary alternatives to existing technologies.[8–10] Since 2008,[11] various research groups have actively begun testing different metals as electrodes (Fe, Cu, Al, Ni, Mg, Pb, Zn, ...) typically using cementitious silicate binders as solid electrolytes. They have employed versatile engineering techniques to create electrochemical devices capable of storing energy, both in the form of batteries[12–16] and, even more broadly, structural supercapacitors.[17–22] It is also worth mentioning recent publications that stand somewhat apart, which focus on the use of cement in Li/S batteries due to its good polysulfide adsorption capability.[23,24]

We note that while both batteries and supercapacitors store energy, batteries rely on faradic redox reactions, enabling higher energy density but slower charge/discharge rates, whereas supercapacitors store energy electrostatically or through surface redox reactions (for pseudocapacitors), offering high power density but lower energy capacity. Despite their potential for long-term energy storage, cement-based batteries remain less explored. Given this gap, our study focuses on advancing cement-type solid batteries for integrated energy storage in construction materials.

One of the most efficient cement-based battery system to date was previously introduced in 2021 by Zhang & Tang,[15] which garnered significant interest from both the scientific

[a.] *Univ. Bordeaux, CNRS, Bordeaux INP, ICMCB, UMR 5026, 33600 Pessac, France.*
[b.] *Present address: Université de Caen Normandie, ENSICAEN, CNRS UMR 6508, CRISMAT, Normandie Univ., 14000 Caen, France. Email : vadim.kovrugin@ensicaen.fr*
[c.] *RS2E, Réseau Français sur le Stockage Electrochimique de l'Energie, FR CNRS 3459, 80039 Amiens Cedex 1, France.*
[d.] *ALISTORE-ERI European Research Institute, CNRS FR 3104, 80039 Amiens Cedex 1, France.*
[e.] *Centro de Física de Materiales (CSIC-UPV/EHU)-Material Physics Centre (MPC), Paseo Manuel de Lardizabal 5, 20018 San Sebastian, Spain, and Donostia International Physics Center, 20018 San Sebastian, Spain*
† Electronic Supplementary Information available: see DOI: 10.1039/x0xx00000x

community and global technology media. Their solution involved using iron and nickel (hydr-)oxides as electrode materials, each of them coated on carbon fiber meshes embedded into a conventional cement-based hardened electrolyte matrix. This rechargeable device demonstrated an impressive energy density, in comparison with previous reports, of approximately 7 Wh/m^2 and 0.8 Wh/L. A very recent evolution of this system has improved its rechargeability to up to 100 cycles.[16]

To shortly overview the performance of cement-based batteries within the broader landscape of electrochemical energy storage, Table 1 presents a comparison of practical voltage and energy density values for different battery technologies. Notably, while cement-based batteries still exhibit significantly lower energy densities than conventional battery chemistries, they hold promise as integrated energy storage solutions within structural materials, as in this case, high energy density is not as critical given the larger volume of the construction itself.

Table 1. Comparison of practical voltage and energy density values across different battery technologies (aqueous, cement, and GP (geopolymer)).

Battery type	Voltage, V	Energy density, Wh/L	Reference
Non-rechargeable batteries			
Alkaline Zn-MnO_2	~1.5	461	[25]
Leclanché	~1.6	165	[25]
Cement-based	~1.0	0.25[a]	[26]
GP-based (OPC+GGFBS)	~1.0	0.04[b]	[27]
Rechargeable batteries			
Li-ion (LCO)	~3.8	570	[25]
Ni-MH	~1.2	235	[25]
Lead-acid	~2.0	70	[25]
GP-based (metakaolin)	~1.3	3.3	This work
Cement-based	~1.0	0.8	[15]

[a] calculated from reported data: V = ~1 V (from plot), t = 25 h, I = ~500 µA (from plot), with a cylindrical cell of 70mm height and 30 mm diameter;

[b] calculated from reported data: V = 1 V, t = 600 s, j = 0.13 mA/cm^2, with a rectangular cell of 70 x 70 x 50 mm^3.

However, when designing such systems, which have the potential to be scaled up significantly in buildings construction given the large volume of cement materials produced annually, sustainability must be a primary consideration from the outset. The traditional cement industry is responsible for about 7% of global CO_2 emissions.[28] In contrast, geopolymers have emerged as promising alternative binders to conventional ordinary Portland cement (OPC) due to their enhanced sustainability, with a potential reduction of CO_2 emissions by 57%.[29] Moreover, compared to OPC, geopolymers exhibit higher ionic conductivity (up to ~10^{-4} S/cm for potassium silicate geopolymer *versus* ~10^{-9} S/cm for conventional OPC[30,31]) and improved mechanical properties (the compressive strength of geopolymers prepared with different aggregates is higher than that of analogous OPC specimens after prolonged exposure[32,33]).

Sustainable cement substitutes representing geopolymers can be various kinds, such as GGBS (ground granulated blast furnace slag), fly ash, rice husk ash, metakaolin etc…[34] Beyond their use as construction materials and their potential for sustainable electrochemical storage applications, geopolymer-based materials have been extensively explored in diverse fields. For example, geopolymers have been investigated for high-temperature applications, including fire-resistant coatings, thermal insulation materials[35] or thermal energy storage devices.[36] In environmental applications, they have shown promise for carbon capture and storage[37], as well as for waste encapsulation and nuclear waste immobilization.[38] Additionally, the tunable porosity of certain metakaolin-based geopolymer formulations makes them promising candidates for filtration, water purification, and as adsorbent materials[39,40]. The integration of geopolymers into electrochemical applications, as proposed in this study, represents an important expansion of their functional scope. By leveraging the intrinsic ionic conductivity and structural stability of geopolymers, this work aims to pave the way for their transition from sustainable construction materials to viable electrochemical energy storage solutions.

2 Results and Discussion

In this communication, we present our solution to the aforementioned challenges of electrochemical storage in cement-like materials using metakaolin geopolymer as a hardened binder electrolyte, with Zn as the negative electrode and MnO_2 as the positive electrode. From the structural point of view, the metakaolin geopolymer is an inorganic binder formed by mixing an aluminosilicate $(Si\text{-}O\text{-}Al\text{-}O)_n$ matrix[32] of calcined kaolin clay with alkaline or acid activation solutions. The precise chemical composition of the used geopolymer was determined by inductively coupled plasma-optical emission spectrometry (see Table S1, ESI†).

Compared to the reported OPC battery with similar chemistry,[12] we adopted a different preparation method. Instead of mixing cementitious binder with Zn and MnO_2 powders to form two solid electrode blocks (*i.e.*, anolyte and catholyte-types, respectively), we first prepared a humid metakaolin (MK) electrolyte paste activated by 2M $ZnSO_4$ solution (with addition of 0.5M $MnSO_4$ in order to suppress the MnO_2 dissolution[41]). Then, the positive electrode was prepared by mixing commercial electrolytic manganese dioxide (EMD) MnO_2, graphite, and polytetrafluoroethylene in a 2 : 1 : 0.15 weight ratio. The mixture was loaded onto a stainless-steel mesh current collector. The prepared positive electrode and a zinc plate serving as the negative electrode were then inserted into the metakaolin-based geopolymer paste (Fig. 1, see Experimental section for details).

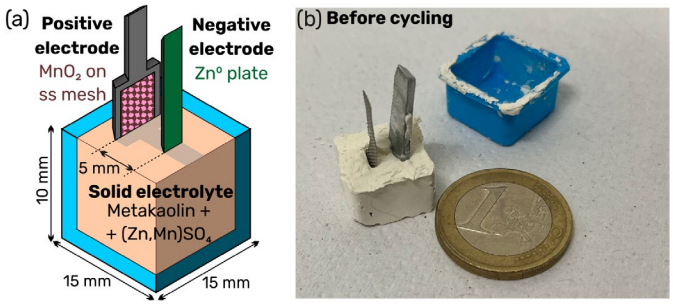

Fig. 1 (a) Scheme of the Zn/MK/MnO_2 cell (ss – stainless steel, see Experimental section for details). (b) Photo of the as-prepared geopolymer cell.

Before evaluating the electrochemical properties of the cells, the ionic conductivity of the as-prepared metakaolin-based geopolymer electrolyte was measured. Electrochemical impedance spectroscopy (EIS) was performed using a two-electrode setup with Pt plate electrodes in freshly prepared cementitious humid pastes. For comparison, aqueous electrolytes were also tested. The corresponding EIS spectra and conductivity values are provided in the ESI† (Figure S1, Table S2). The calculated ionic conductivities revealed that the MK-based paste exhibited a higher conductivity (2.5×10^{-2} S/cm) compared to the OPC-based paste prepared under similar conditions (1.3×10^{-2} S/cm) using the same zinc sulfate aqueous activator solution.

Then, to evaluate electrochemical properties of the Zn/MK/MnO_2 system, cyclic voltammetry (CV) tests were conducted at 0.2 mV/s. Three cells with MK of different curing times – 0, 7, and 28 days – were tested alongside one control cell with the pure liquid electrolyte (*i.e.*, 2M $ZnSO_4$ + 0.5M $MnSO_4$ without added MK powder). The CV curves shown in Fig. 2a for the 5th cycle demonstrate similar behaviour for the three cells with solid electrolyte, whereas the CV profile for the cell with aqueous electrolyte exhibits somewhat more pronounced redox peaks due to higher electrochemical activity in liquid medium. In all cells, the anodic phenomena at around 1.6 V *vs* Zn and with a larger shoulder towards 1.9 V, correspond to the oxidation of manganese, overlapping with the oxygen evolution reaction at higher voltages. The three cathodic peaks centred at around 1.85 V, 1.31 V, and 1.15 V *vs* Zn in the curve obtained for the cell with liquid electrolyte reveal three redox processes occurring during the electrochemical reduction of the MnO_2 electrode. Interestingly, the first peak, R_1, is not clearly visible in the curves obtained for the cells with MK electrolyte. The evolution of the curve shape is shown in Fig. 2b over 30 cycles, where a steady state is observed after about the first 5 cycles. In-between, the electrochemical phenomenon R_1 on the anodic part of the curve decreases over cycling and likely disappears entirely for the batteries with the MK-based electrolyte. To further highlight the presence of R_1 in the initial cycles, we calculated the second derivative (d^2I/dV^2) corresponding to the curvature or concavity of the profile, as shown in the inset of Fig. 2a. This approach helps identify critical points in the measured curve, confirming the existence of R_1 at around 1.9 V *vs* Zn, despite its subtle visibility in the raw data (Fig. S2, ESI†). Moreover, this analysis allowed us to detect a small phenomenon, R'_2. Additional CV data for each cell and different cycles, provided in ESI (Fig. S3-4, ESI†), reveal the same trends.

The discharge capacity of the cells was studied using the galvanostatic cycling with potential limitation (GCPL) technique at C/25. The GCPL profiles for cycle 5 are shown in Fig. 2c, indicating a discharge capacity of about 110 mAh/g of MnO_2 for cells with MK electrolyte when cycling within the 0.3 – 2.1 V *vs* Zn voltage range. This corresponds to an impressive stored energy of 3.3 Wh per liter for the MK solid cell.

As the CV results suggest the presence of several redox reaction steps attributable to different structural transformation mechanisms, three distinct discharge regions can be also distinguished in our GCPL profiles. To more precisely delineate these regions, we have analysed the cathodic derivative curves (dQ/dV) to determine the centres of electrochemical activity: the R_3 (at 0.91 V) and R_2 (at 1.33 V) peaks are clearly visible, while the R_1 phenomenon at a higher voltage may be attributed to a broad shoulder on the curve (Fig. 2c). Interestingly, we also confirm the presence of a small hump at ~1.5 V, denoted as R'_2, whose origin is discussed below in relation to the XRD data. Consequently, the discharge regions were defined as follows: *M1* (2.1 – 1.6 V), *M2* (1.6 – 1.0 V), and *M3* (1.0 – 0.3 V). According to previous reports for the EMD-MnO_2/Zn battery with (Zn,Mn)SO_4 electrolyte,[42,43] these three regions can be attributed to the following electrochemical reactions (Fig. 2d-f):

*M*1: EMD-MnO_2 + $4H^+$ + $2e^-$ ⟶ $Mn^{2+}_{(aq)}$ + $2H_2O$ (MnO_2 dissolution);

*M*2: EMD-MnO_2 + xH^+ + xe^- ⟶ λ-H_xMnO_2 (formation of spinel phase);

*M*3: EMD-MnO_2 + yZn^{2+} + $2ye^-$ ⟶ Zn_yMnO_2 (Zn intercalation into pristine structure).

Therefore, it is unsurprising that the R_1 phenomenon, occurring in the *M*1 region, decreases over time due to the reduced manganese dioxide dissolution process following the cell's hardening process. As a result, the overall contribution of the *M*1 region to the total specific capacity is minimized in MK-based cells, leading to lower specific capacities compared to aqueous systems. Thus, the MK-based system predominantly relies on the electrochemical reactions occurring in the *M*2 and *M*3 regions.

To confirm and elucidate structural changes occurring in the *M2* and *M3* regions, multiple *ex situ* powder X-ray diffraction (XRD) analyses of the electrode and electrolyte materials were conducted at different voltage levels during the electrochemical process. It is important to note that the EMD-MnO_2 material is characterized by low crystallinity and a complex crystal structure considered to be an irregular intergrowth of three alternating polymorphs: β- (pyrolusite), ε- (akhtenskite), and R- (ramdsellite) MnO_2.[44,45] The corresponding simulated XRD patterns are shown in Fig. S5 (ESI†). Consequently, interpreting the XRD results is quite complicated. To carry out accurate phase identification, we simulated (Fig. S6, ESI†) and superposed the powder XRD patterns of various possible phases with the experimental patterns.

This analysis led to several key conclusions. First, the comparison of the XRD patterns recorded between 2.1 V (fully

charged state) and 1.2 V (middle of discharge) after 5 cycles reveals that (1) the XRD peaks of the pristine EMD-MnO_2 do not shift (Fig. S7b-c, ESI†), suggesting no significant structural changes. This indicates that Zn (de-)intercalation into the pristine structure does not occur at higher voltages, as the incorporation of Zn^{2+} cations would inevitably modify the interatomic distances of the crystal structure of the pristine phase. In the same voltage region, secondly (2), new small peaks appear, attributable to the growth of a spinel-type structure. As mentioned earlier, two electrochemical phenomena occurring at ~1.3 and ~1.5 V have been observed in the derivative curves (Fig. 2c). These processes can be attributed to the growth of λ-$H_xMn_2O_4$ and/or $Zn_xMn_2O_4$ (hetaerolite) spinel-type phases, which are difficult to distinguish in our XRD patterns (Fig. S7e-f, ESI†). Moreover, the Zn-containing hetaerolite phase is electrochemically inactive and, once formed, does not participate in the further electrochemical transformations.[46]

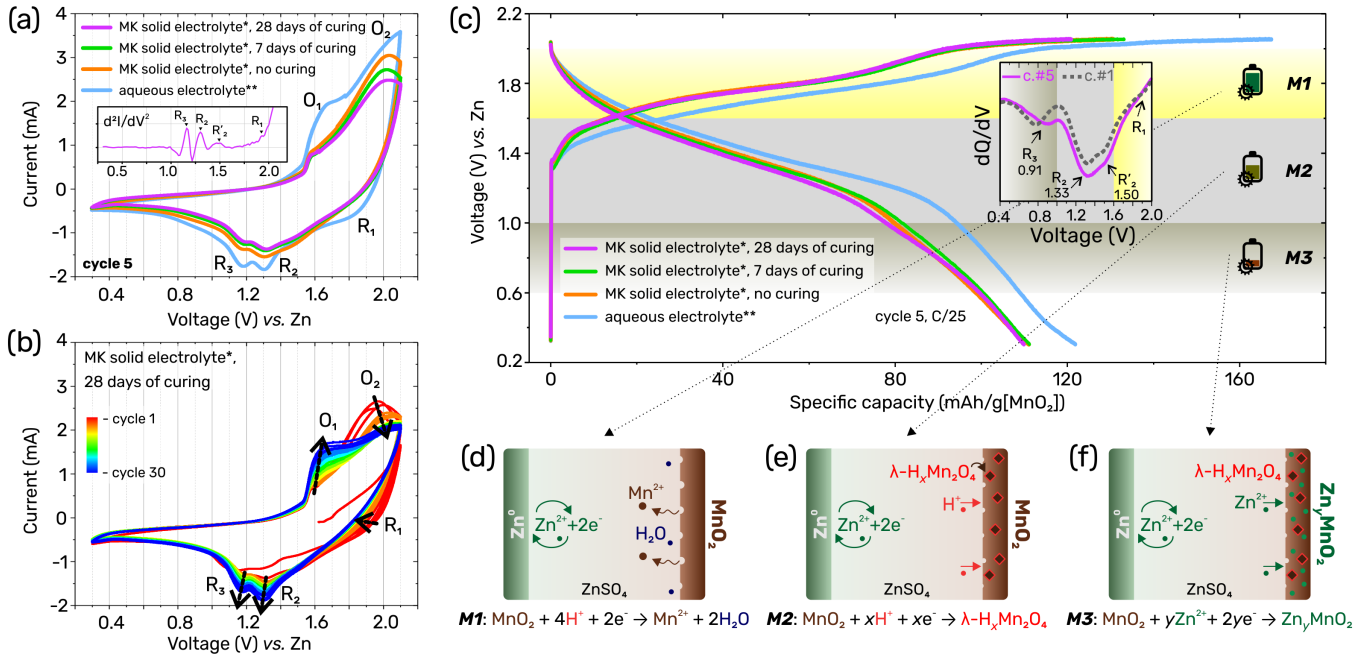

Fig. 2 (a) CV plots for cycle 5 of four cells: * – the solid electrolyte composed of 2M $ZnSO_4$ + 0.5M $MnSO_4$ with metakaolin powder; ** – the liquid electrolyte composed of 2M $ZnSO_4$ + 0.5M $MnSO_4$. The inset shows the second derivative for the curve of the 5th cycle for the battery with MK-based electrolyte with 28-days of curing time. (b) Evolution of the CV plots for the cell with 28-days of curing time. (c) Charge/discharge profiles for the 5th galvanostatic cycle at C/25, with the cathodic derivative curves (dQ/dV) for cycle 5 (magenta) and cycle 1 (dashed grey) shown as an inset for the cell with 28-days of curing time. (d-f) Schematic representation of possible electrochemical mechanisms in the cell.

It is only when the voltage drops further, that we observe a shift in the XRD peaks of the pristine MnO_2 phase towards the smaller 2ϑ-values and higher *d*-values (Fig. 3a and S7d, ESI†). This shift can be associated with the R_3 peak at ~0.9 V on the derivative curve (Fig. 2c) and the incorporation of Zn^{2+} cations into the pristine crystal structure, which leads to the elongation of Mn-O bonds due to the reduction of Mn^{4+} into Mn^{3+}, for charge compensation, and to the growth of EMD-MnO_2 similar tunnel-type Zn_yMnO_2.

The powder XRD analysis of the solid electrolyte is somewhat more straightforward (Fig. 3b and S8, ESI†). The pristine metakaolin powder is characterized by a single intense peak at around 2ϑ ≈ 26.4°, typical for SiO_2. Activation of the geopolymer with $ZnSO_4$ solution results in the formation of well crystallized hexahydrated zinc sulfate, $ZnSO_4(H_2O)_6$, in the solid electrolyte matrix. In the higher voltage range (2.1 – 1.2 V *vs* Zn), no other phases are observed by XRD. However, at lower voltages, metallic zinc and $Zn_4SO_4(OH)_6(H_2O)_5$ start to be detectable. The reversible formation of the latter on the surface of Zn electrodes has also been reported in the literature on aqueous Zn/MnO_2 batteries,[43,47] and it is linked with the decomposition of water into OH^- anions reacting with $ZnSO_4$. The observation of Zn^0 in the metakaolin matrix supports the assumption that Zn^{2+} (de-)intercalation and the diffusion of Zn^{2+} through the electrolyte occur only in the lower voltage range, below 1.2 V *vs* Zn. Thus, our *ex situ* XRD analyses of the solid electrolyte after cycling are in good agreement with the literature reporting on reaction mechanisms in similar aqueous systems.

This allows us to propose the general scheme shown in Fig. 3c for our metakaolin Zn/MnO_2 cell with selected XRD patterns and crystal structures involved in complex electrochemical transformations shown in Fig. 3d-f. For further development, a key issue is to address the activation of the R_1 process (Fig. 2) upon cycling in region *M1*, this one being typically described as driven by the 2-electron/4-proton reductive dissolution of MnO_2 into Mn^{2+}.[42,43] This can lead to unlocking a higher capacity of MnO_2 when more than one electron is electrochemically

activated, as has been recently done, *e.g.*, using a redox mediator in the electrolyte.[48]

To experimentally confirm the occurrence of H^+-(de-)intercalation and Zn^{2+}-(de-)intercalation in different voltage ranges, a series of new cells were cycled in the narrowed voltage range of 2.1 – 1.2 V. In this case, no grey zinc particles were visually observed in the solid electrolyte after cycling, on the contrary to observations made in the extended voltage window between 2.1 and 0.3 V (Fig. S9, ESI†).

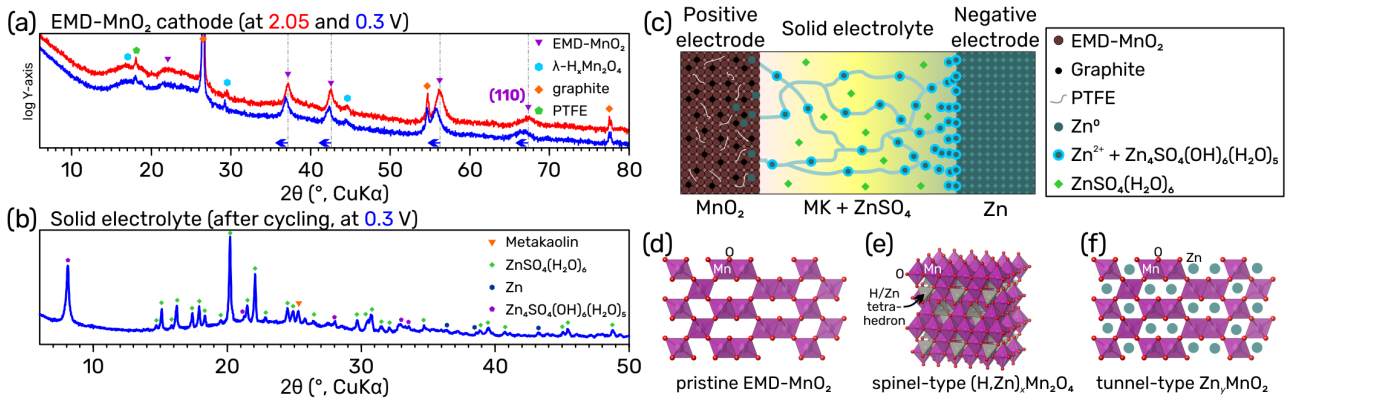

Fig. 3 (a-b) Selected experimental XRD patterns of the electrode and solid electrolyte materials recovered at different voltages upon discharge. (c) Schematic representation of the Zn/MK/MnO_2 cell. (d-f) Crystal structures of the phases involved in the electrochemical transformations.

Furthermore, as clearly seen in Fig. S9a (ESI†), mechanical durability of the hardened geopolymer blocks upon repetitive charge/discharge cycles is an issue, as shown by the surface cracking of the cell. These mechanical degradations could be associated to volume changes induced by Zn^{2+}-(de-)intercalation overtime, likely influenced by side reactions at the Zn electrode interface. Zinc metal is known to react with cementitious materials, forming calcium zincate and undergoing hydrogen evolution reaction (HER), which may induce local stresses.[49] Unlike the predominantly alkaline conditions of standard concrete, our system operates in a mild acidic electrolyte (pH 6-7), where zinc remains in its ionic form (Zn^{2+}) without forming an oxide passivation layer, allowing for reversible plating/stripping and ensuring the rechargeability of our cell. Meanwhile, HER remains inevitable due to its overpotential, which thermodynamically precedes zinc redeposition. Indeed, a simplified estimation using the Nernst equation under conditions of pH = 6 and $[Zn^{2+}]$ = 2 mol/L gives redox potentials of approximately -0.35 V vs. SHE for $2H^+ + 2e^- \rightarrow H_2$ and -0.75 V vs. SHE for $Zn^{2+} + 2e^- \rightarrow Zn$, confirming that HER occurs first. This HER reaction, along with the formation of hexahydrated zinc sulfate as a side product, compromises the negative electrode / metakaolin interface, leading to crack formation. Consequently, this degradation results in a decrease in cyclability after the first 10 cycles metakaolin cells cured before testing for 28 days (Fig. 4a), and in final cell failure due to the loss of mechanical integrity. A number of studies in the literature have already explored strategies to mitigate such side reactions and control the HER, including surface coatings, electrolyte additives.[50]

Cells with shorter curing times perform better, likely because not all inner hardening processes had been completed before cycling. As shown in Fig. 4b, capacity retention can be improved if the cut-off voltage is limited at 1.2 V *vs* Zn, in good agreement with the participation of only small H^+ ions in charge transfer and thus to better mechanical integrity of the geopolymer blocks. However, this reduces the discharge capacity by about half (Fig. 4b). To mitigate the participation of Zn into redox processes, we launched a series of cells with a cut-off voltage of 0.8 V *vs* Zn (Fig. S10 and S11, ESI†). Smoother capacity fading upon electrochemical cycling was observed, with capacity and energy densities limited to 30 mAh/g and 0.9 Wh/L, respectively, after 30 cycles (Fig. 4b and S10b, ESI†).

The comparison of the electrochemical performance of the cell at different current rates for the geopolymer with 28-days of curing time is summarized in Fig. S12 (ESI†). It is worth highlighting that despite the aforementioned issues, the cell exhibits good capacity retention when switching between different C-rates. Furthermore, the volumetric energy density of the cells reported in this communication significantly surpasses, to the best of our knowledge, all cement-like batteries reported in the literature with comparable data: our 3.3 Wh/L of the geopolymer block *versus* about 0.8 Wh/L.[15,16]

To evaluate the impact of temperature on cycling stability, additional experiments were conducted at 30 °C, 40 °C, and 50 °C (Fig. 4c). The results indicate that cells tested at higher temperatures exhibit a pronounced peak in energy density at the very beginning, reaching significantly higher values than at 23 °C (5.7 Wh/L at 50 °C). However, this is followed by a rapid decline accelerating performance degradation and leading to negligible energy density after 8 cycles. This behaviour can be attributed to increased ionic conductivity but reduced structural integrity: while higher temperatures enhance ion transport within the electrolyte, they also accelerate degradation reactions at the electrode/metakaolin interface, compromising cycling stability. Additionally, water loss at

elevated temperatures likely promotes dehydration, increasing internal resistance and causing expansion/contraction mismatches between the solid matrix and electrode active materials, which induces mechanical stress and contact loss. These findings underscore the need for thermal management strategies or electrolyte modifications to improve the temperature resilience of metakaolin-based batteries.

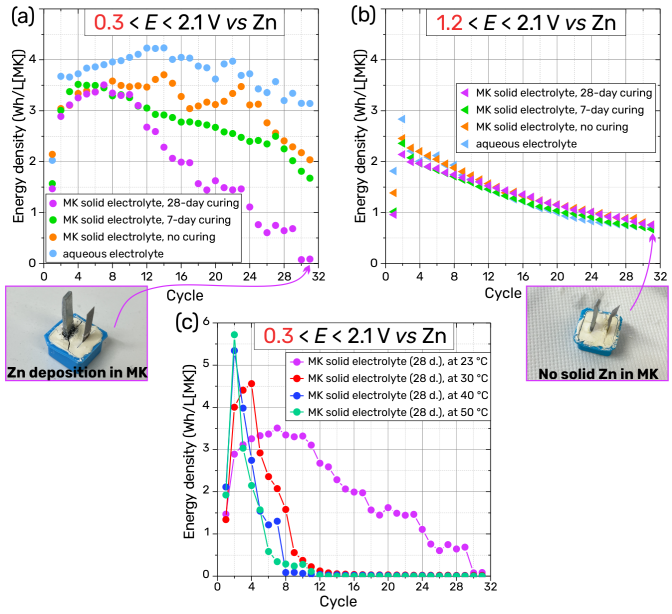

Fig. 4 Energy density (in Wh/L of MK block) as a function of cycle number at room temperature in the (a) 0.3–2.1 V vs Zn range and (b) 1.2–2.1 V vs Zn range; (c) comparison of cycling performance at different temperatures.

Given the potential application of our material in construction, its mechanical strength is also a crucial factor. To gain initial insights, we measured the Vickers hardness (HV), which is well-established and non-destructive method to determine the local mechanical properties of cementitious materials.[51,52] The measured HV0.1 of 84.7 N/mm^2 suggests that the current formulation remains relatively brittle compared to reported values for hardened cement pastes[52] and geopolymers[53] ~200 or sulfate-corroded cements ~110.[54]

Additionally, to evaluate the material's hydration and drying behaviour, we monitored mass loss over time. After about 40 days of curing, our cells retained only 65% of their initial mass (activator-to-metakaolin ratio of 1.1), indicating significant free water loss compared to literature reports (Fig. S13, ESI†): *e.g.*, 87.2% of the initial mass retained with a water-to-metakaolin ratio of 0.65.[55] This trend also aligns with our electrochemical observations, where capacity fading occurred after 10 cycles – approximately 38 days in total (28 days of curing followed by 10 days of electrochemical cycling) – coinciding with the complete loss of free water. These results suggest that the presence of liquid solution is essential for the functionality of the cell in this state. However, the high water content likely increases porosity, potentially reducing mechanical integrity. These findings emphasize the need for further optimization of the formulation and curing process to enhance both mechanical stability and durability. To address these challenges, potential strategies include adjusting the curing conditions to better control water retention, incorporating hydrophilic additives to sustain ionic conductivity, or designing self-replenishing electrolyte systems. Future work will focus on improving these aspects to make the material more suitable for real structural applications.

From an application perspective, deploying such batteries in humid environments – such as tropical climates or infrastructure exposed to constant moisture (*e.g.*, bridges or tunnels) – could naturally help sustain the liquid phase, reducing electrolyte loss and improving long-term cycling stability. Furthermore, integrating a modular design approach, where battery components are structured in accessible layers or compartments, could facilitate maintenance and potential replacement without compromising the structural integrity of the construction. Such approaches will be crucial for ensuring long-term functionality while maintaining both electrochemical performance and mechanical durability.

The concept realization of two of our cells connected in series is illustrated in Fig. 5, and S14 (ESI†), demonstrating the illumination of LEDs in a small wooden toy house with forward voltages ranging about 2 to 3.5 V, depending on the light-emitting colours.

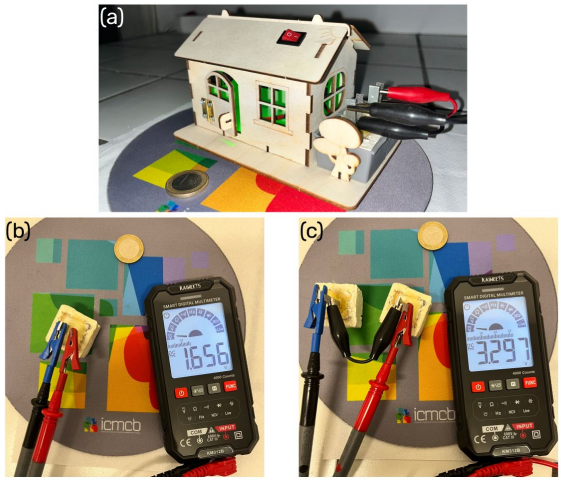

Fig. 5 (a) Powering a green LED. (b) Operating potential at the charged state of one cell. (c) Operating potential of two cells connected in series.

3 Experimental

Materials

All chemicals were used as received, without further purification. For the preparation of positive electrodes, graphite (LONZA KS-44) and powdered polytetrafluoroethylene (>40 µm, Sigma-Aldrich) were used. Electrolytic manganese dioxide MnO_2 (10 µm, reagent grade, ≥ 90%, Sigma-Aldrich) served as the active material for the positive electrode. A stainless steel mesh (100 mesh, 0.15 mm hole size, 0.6 mm thickness) purchased from Thermo Scientific Chemicals was used as the current collector. Zinc metal foil (1.6 mm thickness, Alfa-Aesar)

was employed as the negative electrode. For the preparation of the solid electrolyte, a commercially available metakaolin geopolymer (Moertelshop, Backstein Engineering GmbH) and ordinary Portland cement CEM I-42.5R (Povazska Cementaren a.s., Ladge, Slovakia) were used. The activation solution was prepared using $ZnSO_4 \cdot 7H_2O$ (Alfa Aesar, 98%) and $MnSO_4 \cdot H_2O$ (Sigma-Aldrich, 99%).

Battery preparation method

To date, researchers have adopted two fundamental designs for cement-based batteries: (i) the classic probe-style configuration, where two electrodes are embedded in a cementitious electrolyte matrix, and (ii) a layered configuration, in which a cement-based electrolyte layer is sandwiched between cement-based anode and cathode layers. Following the more traditional probe-style approach, our cell design consists of two electrodes inserted into a solid metakaolin matrix.

For the electrolyte preparation, a 2M $ZnSO_4$ solution was first prepared, with the addition of 0.5M $MnSO_4$. This solution was then used to activate the metakaolin geopolymer. The metakaolin powder was mixed with the activation solution at a 1.1 weight ratio using a vortex mixer. Notably, such a high powder-to-solution ratio was necessary to achieve the desired consistency of the metakaolin paste. We note also that when using an alkaline activation solution, however, a lower ratio of 0.6 is sufficient to obtain a paste of similar consistency. Soft silicone molds ($15 \times 15 \times 10$ mm^3) were used, into which the metakaolin paste was cast.

For the preparation of the positive electrode, a stainless steel grid current collector in an upside-down 'T' shape was employed, with a working electrode rectangular area of 12.5×7.6 mm^2. The positive electrode composite was prepared by mixing in an agate mortar commercial EMD-MnO_2 with graphite and polytetrafluoroethylene in a 2 : 1 : 0.15 weight ratio to produce a 'rubbery' material. The mixture was then loaded onto the stainless steel grid and pressed at 4 t/cm^2. An active material loading of the electrodes was about 47 mg/cm^2. The Zn foil serving as the negative electrode, cut to 25×5 mm^2, was cleaned with ethanol without additional polishing.

The two electrodes were then inserted into the metakaolin-based geopolymer paste, maintaining a 5 mm separation. This distance was ensured by a plastic cup with two holes for the electrodes, which prevented them from shifting before the paste reached sufficient density. The as-prepared cell with the cup was then placed in a sealed plastic container and stored at ambient temperature (22°C) during the hydration process until testing started.

Characterization techniques

Powder X-ray diffraction (XRD) analyses were performed at room temperature using a PANalytical X'Pert Pro diffractometer (The Netherlands) equipped with an X'Celerator detector (Cu Kα radiation, λ = 1.5405 Å). Data were collected with a step size of 0.017° for 1.23 s per step over a 2ϑ range of 8–80°, with an acquisition time of approximately 1.5 hours per pattern. XRD profile analysis was conducted using the PANalytical HighScore Plus software.

Electrochemical studies were carried out using a Biologic VMP potentiostat (France) operated through EC-Lab software. Cyclic voltammetry (CV) measurements were performed at a scan rate of 0.2 mV/s within a voltage range of 0.3 to 2.1 V vs. Zn. Galvanostatic charge/discharge voltage profiles were recorded at a cycling rate of C/25 over different voltage ranges. The theoretical capacity (C) was calculated based on one electron per Mn in the electrode, with the exact Mn content determined through chemical analysis. Various current rates were also tested to evaluate rate performance under faster charge/discharge conditions. Electrochemical impedance spectroscopy (EIS) measurements were conducted over a frequency range of 1 MHz to 100 kHz with a signal amplitude of 10 mV to compare the total conductivity of various electrolytes. For calibration, a 0.1 M KCl aqueous standard solution was measured under identical experimental conditions. The intersection of the EIS curve with the real axis was used to determine the bulk resistance of the electrolyte. The ionic conductivity was then calculated using the equation: $\sigma = d/(S \times R_b)$, where d is the distance between the two electrodes (cm), S is the contact area of the electrolyte with the electrode (cm^2), and R_b is the bulk resistance (Ohm).

The chemical composition of the commercial metakaolin and the precise Mn content of the commercial manganese dioxide were determined using inductively coupled plasma-optical emission spectrometry (ICP-OES) with an Agilent 5800 spectrometer (U.S.A.). The samples were prepared by dissolving approximately 10 mg of powder in a solution of acids (HNO_3 : HCl : HF) in a volumetric ratio of 2 : 1 : 1. The mixtures were heated using an Anton Paar Multiwave Pro microwave oven to ensure complete dissolution of the powder. To achieve a target element concentration between 1 and 50 mg/L, the solutions were diluted by adding deionized water. The resulting solution was then introduced into a nebulization chamber, where it was combined with an argon flow to create an aerosol. Five measurements were taken for each sample to ensure accuracy.

Hardness measurements were performed using a ZHVμ-S Micro Vickers hardness tester (Zwick Roell, Germany). The Vickers hardness (HV) test was conducted on a laterally smooth surface of the demolded solid metakaolin cell after 28 days of curing. A diamond square pyramid indenter with a conical angle of 136° was applied with a load of 0.1 kgf for 15 s. After unloading, the Vickers hardness was determined by measuring the diagonal length of the indentation using the following equation: $HV = 1.8544 \times F/d^2$, where HV is the Vickers hardness, F is the applied load (N), and d is the average diagonal length (mm) of the indention optically measured for each test. The reported HV value represents the average of three indentation measurements.

4 Conclusions

The technology presented in this communication represents another step towards paving the way for new large-scale

sustainable energy storage applications. Given the limited studies on battery applications using cements or geopolymers, our work extends this discussion to cementitious-based batteries in general. The superior performance of our system can be attributed to several key factors: the use of metakaolin as the geopolymer precursor, instead of ordinary Portland cement, enhances ionic conductivity. The activation of metakaolin with a neutral $ZnSO_4$ solution, rather than the conventional alkaline activators used in construction applications, likely improves ionic transport. Furthermore, the retention of a liquid electrolytic phase within the metakaolin matrix ensures efficient charge transfer, which is crucial for battery stability and rechargeability. However, further intensive research and development are required to address technical challenges, such as improvement of mechanical properties of solid metakaolin electrolyte and addressing multiples issues with zinc electrodes, which are widely studied and reported in the literature. These approaches may include the development of surface coatings for Zn negative electrodes and/or the use of electrolyte additives. Additionally, incorporating flexible binders into the metakaolin-based matrix could help accommodate volume changes without compromising mechanical integrity. By advancing this technology, we move towards a greener and more resilient future.

Conflicts of interest

The authors declare no competing financial interest

Data availability

The data supporting this article have been included as part of the Electronic Supporting Information (ESI†). The authors have cited additional references within the ESI.[56–66]

Acknowledgements

This work was carried out within the framework of the LTC Green Concrete project. The authors also acknowledge the French National Research Agency (STORE-EX Labex Project ANR-10-LABX-76-01) for its financial support. We extend our thanks to Fabien Palencia, Catherine Denage, and Eric Lebraud for their technical assistance. We also thank Valentina Musumeci for her early contributions in conceptualizing the initial ideas. Additionally, we appreciate the financial support provided by CNRS, Bordeaux INP, and the Region Nouvelle-Aquitaine.

Notes and references

1 N. Aschan, *Mag. Concr. Res.*, 1966, **18**, 153–160.
2 J.-M. Tarascon, *Nat. Mater.*, 2022, **21**, 979–982.
3 J. Amici, P. Asinari, E. Ayerbe, P. Barboux, P. Bayle-Guillemaud, R. J. Behm, M. Berecibar, E. Berg, A. Bhowmik, S. Bodoardo, I. E. Castelli, I. Cekic-Laskovic, R. Christensen, S. Clark, R. Diehm, R. Dominko, M. Fichtner, A. A. Franco, A. Grimaud, N. Guillet, M. Hahlin, S. Hartmann, V. Heiries, K. Hermansson, A. Heuer, S. Jana, L. Jabbour, J. Kallo, A. Latz, H. Lorrmann, O. M. Løvvik, S. Lyonnard, M. Meeus, E. Paillard, S. Perraud, T. Placke, C. Punckt, O. Raccurt, J. Ruhland, E. Sheridan, H. Stein, J. Tarascon, V. Trapp, T. Vegge, M. Weil, W. Wenzel, M. Winter, A. Wolf and K. Edström, *Adv. Energy Mater.*, 2022, **12**, 2102785.
4 D. D. L. Chung and X. Xi, *Ceram. Int.*, 2023, **49**, 24621–24642.
5 J. Bravo, A. Abdulridha, S. Wang, D. Matrone, Z. Yao, S. Neti, C. Naito, S. Quiel, M. Suleiman and C. Romero, *Energy*, 2023, **277**, 127670.
6 G. Goracci, M. B. Ogundiran, M. Barzegar, A. Iturrospe, A. Arbe and J. S. Dolado, *ACS Omega*, 2024, **9**, 13728–13737.
7 M. Barzegar, G. Goracci, P. Martauz and J. S. Dolado, *Constr. Build. Mater.*, 2024, **411**, 134398.
8 A. Sundaramoorthi and P. Thangaraj, *J. Eng. Appl. Sci.*, 2023, **70**, 39.
9 B. A. Salami, T. A. Oyehan, A. Tanimu, A. B. Olabintan, M. Ibrahim, M. O. Sanni-Anibire, S. A. Nafiu, O. Arowojolu and T. A. Saleh, *Environ. Chem. Lett.*, 2022, **20**, 1671–1694.
10 D. N. Bangera, S. Y. N. and R. A. Nazareth, *RSC Adv.*, 2024, **14**, 28854–28880.
11 G. T. Burstein and E. I. Speckert, *ECS Trans.*, 2008, **3**, 13–20.
12 Q. Meng and D. D. L. Chung, *Cem. Concr. Compos.*, 2010, **32**, 829–839.
13 A. Byrne, S. Barry, N. Holmes and B. Norton, *Adv. Mater. Sci. Eng.*, 2017, **2017**, 1–14.
14 N. I. M. Nadzri, N. M. Amin and M. F. Arshad, *J. Mech. Eng.*, 2021, **10**, 1–16.
15 E. Q. Zhang and L. Tang, *Buildings*, 2021, **11**, 103.
16 L. Yin, S. Liu, D. Yin, K. Du, J. Yan, C. K. Armwood-Gordon and L. Li, *J. Energy Storage*, 2024, **93**, 112181.
17 H. Wang, Y. Diao, Y. Lu, H. Yang, Q. Zhou, K. Chrulski and J. M. D'Arcy, *Nat. Commun.*, 2020, **11**, 3882.
18 C. Fang and D. Zhang, *J. Mater. Chem. A*, 2020, **8**, 12586–12593.
19 J. V. Vaghasiya, C. C. Mayorga-Martinez and M. Pumera, *Adv. Funct. Mater.*, 2021, **31**, 2106990.
20 J. Wang and D. Zhang, *Mater. Chem. Phys.*, 2022, **277**, 125488.
21 N. Chanut, D. Stefaniuk, J. C. Weaver, Y. Zhu, Y. Shao-Horn, A. Masic and F.-J. Ulm, *Proc. Natl. Acad. Sci.*, 2023, **120**, e2304318120.
22 J. Wang, P. Zhan and D. Zhang, *Cem. Concr. Compos.*, 2023, **138**, 104987.
23 Y.-J. Wang, C.-C. Hung and S.-H. Chung, *Ceram. Int.*, 2023, **49**, 11846–11853.
24 T.-M. Hung, C.-C. Wu, C.-C. Hung and S.-H. Chung, *Nanomaterials*, 2024, **14**, 384.
25 T. B. Reddy and D. Linden, Eds., *Linden's Handbook of Batteries*, The McGraw-Hill Companies, Inc, 4th edn., 2011.
26 G. Qiao, G. Sun, H. Li and J. Ou, *Appl. Energy*, 2014, **131**, 87–96.
27 Y.-H. Chen, S.-C. Lin, J.-A. Wang, S.-Y. Hsu and C.-C. M. Ma, *J. Electrochem. Soc.*, 2018, **165**, A3029–A3039.
28 Supriya, R. Chaudhury, U. Sharma, P. C. Thapliyal and L. P. Singh, *J. Clean. Prod.*, 2023, **417**, 137466.
29 G. Bumanis, A. Korjakins and D. Bajare, *Environments*, 2022, **9**, 6.
30 M. Saafi, A. Gullane, B. Huang, H. Sadeghi, J. Ye and F. Sadeghi, *Compos. Struct.*, 2018, **201**, 766–778.
31 W. Yao, G. Xiong, Y. Yang, H. Huang and Y. Zhou, *Constr. Build.*

Mater., 2017, **150**, 825–832.
32 C.-K. Ma, A. Z. Awang and W. Omar, *Constr. Build. Mater.*, 2018, **186**, 90–102.
33 K. Kupwade-Patil and E. N. Allouche, *J. Mater. Civ. Eng.*, 2013, **25**, 131–139.
34 S. Patil, D. Joshi, D. Mangla and I. Savvidis, *Mater. Today Proc.*, , DOI:10.1016/j.matpr.2023.04.046.
35 J. Temuujin, W. Rickard, M. Lee and A. van Riessen, *J. Non. Cryst. Solids*, 2011, **357**, 1399–1404.
36 M. Rahjoo, G. Goracci, P. Martauz, E. Rojas and J. S. Dolado, *Sustainability*, 2022, **14**, 1937.
37 N. M. Faqir, S. Elkatatny, M. Mahmoud and R. Shawabkeh, *Appl. Clay Sci.*, 2017, **141**, 81–87.
38 M. Houhou, N. Leklou, H. Ranaivomanana, J. Penot and S. de Barros, *Discov. Appl. Sci.*, 2025, **7**, 126.
39 C. Bai, K. Zheng, F. Sun, X. Wang, L. Zhang, T. Zheng, P. Colombo and B. Wang, *Appl. Clay Sci.*, 2024, **258**, 107490.
40 S. C. Tarantino, R. Occhipinti, F. Maraschi, M. Zema, M. P. Riccardi, A. Profumo and M. Sturini, *Appl. Clay Sci.*, 2024, **259**, 107502.
41 S. H. Kim and S. M. Oh, *J. Power Sources*, 1998, **72**, 150–158.
42 D. Chao, W. Zhou, C. Ye, Q. Zhang, Y. Chen, L. Gu, K. Davey and S. Qiao, *Angew. Chemie*, 2019, **131**, 7905–7910.
43 I. Aguilar, P. Lemaire, N. Ayouni, E. Bendadesse, A. V. Morozov, O. Sel, V. Balland, B. Limoges, A. M. Abakumov, E. Raymundo-Piñero, A. Slodczyk, A. Canizarès, D. Larcher and J.-M. Tarascon, *Energy Storage Mater.*, 2022, **53**, 238–253.
44 C.-H. Kim, Z. Akase, L. Zhang, A. H. Heuer, A. E. Newman and P. J. Hughes, *J. Solid State Chem.*, 2006, **179**, 753–774.
45 D. E. Simon, R. W. Morton and J. J. Gislason, *Adv. X-ray Anal. JCPDS*, 2014, **47**, 267–280.
46 J. Shin, J. K. Seo, R. Yaylian, A. Huang and Y. S. Meng, *Int. Mater. Rev.*, 2020, **65**, 356–387.
47 Z. Li, Y. Li, X. Ren, Y. Zhao, Z. Ren, Z. Yao, W. Zhang, H. Xu, Z. Wang, N. Zhang, Y. Gu, X. Li, D. Zhu and J. Zou, *Small*, 2023, **19**, 2301770.
48 J. Lei, Y. Yao, Z. Wang and Y.-C. Lu, *Energy Environ. Sci.*, 2021, **14**, 4418–4426.
49 X. G. Zhang, *Corrosion and Electrochemistry of Zinc*, Springer US, Boston, MA, 1996.
50 Q. Li, L. Han, Q. Luo, X. Liu and J. Yi, *Batter. Supercaps*, 2022, **5**, e202100417.
51 S. Igarashi, A. Bentur and S. Mindess, *Adv. Cem. Based Mater.*, 1996, **4**, 48–57.
52 M. A. Glinicki and M. Zielinski, *Cem. Concr. Res.*, 2004, **34**, 721–724.
53 M. Lizcano, H. S. Kim, S. Basu and M. Radovic, *J. Mater. Sci.*, 2012, **47**, 2607–2616.
54 H. Chu, T. Wang, L. Han, L. Cao, M.-Z. Guo, Y. Liang and L. Jiang, *Constr. Build. Mater.*, 2021, **309**, 125119.
55 Q. Tian, *Ceram. - Silikaty*, 2022, **66**, 236–244.
56 S. Scherb, M. Köberl, N. Beuntner, K.-C. Thienel and J. Neubauer, *Materials (Basel).*, 2020, **13**, 2214.
57 Y. Jiang, L. Yuan, X. Wang, W. Zhang, J. Liu, X. Wu, K. Huang, Y. Li, Z. Liu and S. Feng, *Angew. Chemie Int. Ed.*, 2020, **59**, 22659–22666.
58 I. J. Bear, I. E. Grey, I. C. Madsen, I. E. Newnham and L. J. Rogers, *Acta Crystallogr. Sect. B Struct. Sci.*, 1986, **42**, 32–39.
59 N. Curetti, D. Bernasconi, P. Benna, G. Fiore and A. Pavese, *Phys. Chem. Miner.*, 2021, **48**, 43.
60 J. E. Post and P. J. Heaney, *Am. Mineral.*, 2004, **89**, 969–975.
61 P. Patra, I. Naik, H. Bhatt and S. D. Kaushik, *Phys. B Condens. Matter*, 2019, **572**, 199–202.
62 B. Ammundsen, D. J. Jones, J. Rozière, H. Berg, R. Tellgren and J. O. Thomas, *Chem. Mater.*, 1998, **10**, 1680–1687.
63 T. Kohler, T. Armbruster and E. Libowitzky, *J. Solid State Chem.*, 1997, **133**, 486–500.
64 J. E. Post and D. E. Appleman, *Am. Mineral.*, 1988, **73**, 1401–1404.
65 A. S. Masadeh, M. T. M. Shatnawi, G. Adawi and Y. Ren, *Mod. Phys. Lett. B*, 2019, **33**, 1950410.
66 M. Spiess and R. Gruehn, *Zeitschrift für Anorg. und Allg. Chemie*, 1979, **456**, 222–240.